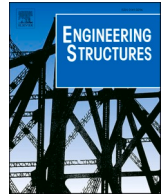# Two-dimensional strain field analysis of reinforced concrete D-regions based on distributed optical fibre sensors

N.B. When citing this work, cite the original published paper.

(article starts on next page)

Two-dimensional strain field analysis of reinforced concrete D-regions based on distributed optical fibre sensors

Ignasi Fernandez [a],[*], Carlos G. Berrocal [a],[b], Rasmus Rempling [a],[c]

[a] *Chalmers University of Technology, Division of Structural Engineering, Gothenburg SE-41296, Sweden*
[b] *Thomas Concrete Group AB, Södra Vägen 28, Gothenburg 412 54, Sweden*
[c] *NCC Sverige AB, Sweden*

ARTICLE INFO

ABSTRACT

The introduction of Distributed Optical Fibre Sensing in experimental testing of reinforced concrete structures has enabled the acquisition of measurements with an unparalleled level of detail, providing an accurate and ubiquitous description of cracking and deflections throughout an element. However, most of the available research using this technology has focused on the study of beam specimens and high quality data for the calibration and development of models that can describe accurately the behaviour of D-regions in service is still lacking. For that reason, the application of distributed optical fibre sensing in D-regions remains a subject of interest. In this work a method for the deployment of fibre sensors in a multilayer configuration is presented for a wall element. An interpolation approach is then proposed, which combined with the distributed nature of the sensors enabled the description of detailed heat maps for the global and principal strain fields. The results indicated that shear strains can reveal the position of shear cracks well before they are formed whereas the maximum and minimum principal strains clearly show the crack pattern and crack development as well as the load transfer mechanisms including, for the first time, the experimental identification of a secondary strut-and-tie mechanisms.

1. Introduction

Despite concrete being one the most employed materials in construction, the design of reinforced concrete structures is complex and presents important challenges that still need to be addressed. A concrete structure can be often divided in distinctive regions that require different design approaches due to their behaviour under loading. These regions are well known as Beam regions (B-regions) and Disturbed regions (D-regions). The main difference between both is the distribution of strains in the cross-section. In B-regions the bending effect can be simplified assuming a strain field normal to the concrete section, where the contribution of the shear strains is neglected, meaning that Bernoulli's theory can be applied and used for design and assessment. Conversely, D-regions present more complex strain fields being the shear deformations nonnegligible in the response of the region. Common examples of D-regions in a concrete structure are corner joints between columns and beams, support corbels, foundations, walls, or beams where the length to height ratio is low, widely known as deep beams. The existence of such regions has been long known and the methods for their design and analysis are long-standing. However, due to the intrinsic complexity, geometry variability and material dependency of D-regions, a single unified design method is not available. Nevertheless, two methods are widely used for the design and detailing of D-regions: the strut-and-tie method and the stress field method. Both methods are based on the lower bound theorem of plasticity, although their origin is rooted in different approaches. Essentially the strut-and-tie method is based on the truss analogy, aiming to provide an intuitive phenomenological description of the reinforced concrete behavior after cracking without any theoretical basis [1–3]. Conversely stress field methods arose as a direct application of the theory of plasticity, the application of which in concrete structures dates back to 1961 by Drucker [4]. An initial approach for using the stress field method was proposed by the Danish Society of Structural Science and Engineering [5]. Later Muttoni et al. [6] presented a more general methodology, which already included serviceability aspects. In a further step, a finite element approach to the problem combining linear elasticity and pre-set states of stresses accounting for the condition of plasticity in the elements was presented by Despot [7]. A generalization of the later was proposed by Ruiz et al. [8] and further developed by Muttoni et al. [9], where a finite element analysis including steel non-linearities and concrete plasticity

---

* Corresponding author.

was established to describe the stress field and later used for both analysis and design of D-regions. However, in spite of the potential of the stress field methods, a major drawback is still the difficulties to evaluate D-regions in Serviceability Limit State (SLS), relegating existing methods to the design in Ultimate Limit State (ULS). Consequently, some efforts have been directed towards the development of methods that address Service Limit State evaluations [10,11]. The current development of either strut-and-tie or stress field methods is based on wide experimentation. However, even though the current state-of-the-art consists of an extensive database of concrete elements of different configurations, the limited data obtained from the tests due to the utilization of traditional instrumentation represents an important limitation for the study of D-regions. Such data is often limited to hand-measured crack widths at discrete load levels, the description of crack patterns only at failure, load displacement curves for a single point of the structure and the geometrical and loading configuration of the specimens [12–20].

In the last years, new sensing technologies and instrumentation techniques have been developed and introduced to the structural engineering testing scene, such as Digital Image Correlation (DIC) or strain and temperature measurement based on optical fibre sensing. Particularly, optical fibre sensors present several advantages compared to traditional sensors, them being small in size, light weight, chemically inert and corrosion resistant and immune to electromagnetic fields [21]. In this context Fibre Bragg Grating and Fabry-Perot have been widely researched and to date are the most used type of optical fibre measurements in practice [22]. However, these two types of sensors have clear limitations with respect to the maximum number of measuring points along an optical fibre and their spacing, thus being often referred to as quasi-distributed sensors, making them less suitable for specific applications such as crack detection in concrete structures.

More recently, Distributed Optical Fibre Sensors (DOFS) featuring unprecedented spatial resolutions have been developed, thereby opening for new possibilities in the development of testing techniques. The working principle of DOFS is based on the analysis of light backscattering that occurs along the fibre due to three different processes: Raman, Brillouin and Rayleigh scattering. Raman scattering is highly sensitive to temperature variations and consequently its application has been mostly limited to fields other than civil engineering [23]. Brillouin and Rayleigh scattering, on the other hand, are both sensitive to temperature and strain variations, yet they present fundamental differences with respect to spatial resolution and measuring range. Indeed, DOFS based on Brillouin Optical Time Domain Reflectometry (BOTDR) feature a spatial resolution in the order of the tens of centimetres [24] but their measuring range can reach lengths of up to 300 km [25]. Conversely, the sensing range of Rayleigh based DOFS is currently limited to 100 m, but they boast an unmatched spatial resolution in the sub-millimetric scale [26].

Owing to such capabilities, as indicated in a review on the use of DOFS in civil engineering conducted by Bado et al. [27] the application of DOFS spans from geotechnical applications, tunnel lining, pipes, wind turbines or different applications within the built environment. Yet, as the use of DOFS for structural engineering purposes is still rather young compared to other more traditional instrumentation technologies, large efforts are currently devoted to increase the usability of such technology and broaden the possibilities of its application through laboratory experimentation. As a result of those investigations, the suitability of DOFS for the evaluation of key performance indicators has been demonstrated experimentally for both Brillouin-based DOFS [28–31] and Rayleigh-based DOFS [32–37]. Significant efforts have been carried out for the assessment of crack widths using Rayleigh-based DOFS grounded directly on the shape of the strain measurements performed without the use of strain transfer models between the fibre core and the substrate element, both for short and long-term monitoring [38–41].

Despite very promising results, most of the available research has been limited to the study of simple elements such as beams. Due to the relatively low level of maturity of DOFS within structural engineering

applications, studies in the literature scoping more ambitious applications and complex elements such as D-regions are scarce. In this regard, Rodriguez et al. [42,43], presented two experimental campaigns which successfully assessed and evaluated both crack widths and crack patterns in a D-region of a beam based on DOFS measurements. In more recent studies Mata-Falcón et al. [44] and Poldon et al. [36,45,46], presented a combined acquisition technique based on DIC and DOFS attached to a steel reinforcement grid for the successful evaluation of the tensional state of the steel bars in elements subjected to shear deformations. In a work carried out by Battista et al. [47] DOFS sensors based on Brillouin technology were deployed in a wall-diaphragm element, aiming to study the out of plane deflections during construction. In a later study [48], sensors were arranged in a grid configuration to study the concrete behaviour of a strong floor slab during casting, combining Brillouin-DOFS and Fibre Bragg Grating solutions, both for temperature and strain measurements. Yet, the applicability of DOFS for the study of strain fields in wall elements has not yet been explored, which opens the possibility of broadening the understanding of the structural behaviour of disturbed regions under SLS, and not only under ULS as it is commonly done, as well as to validate the new methods for design and assessment.

This paper reports the results of an investigation of the suitability and performance of robust fibre optic cables to evaluate strain fields under different load levels in D-regions. In particular, the work focuses on the analysis of Rayleigh scattering based DOFS measurements with sensors deployed in a three-directional grid configuration in the mid-plane of a wall element. The study presents a method for the sensor deployment and postprocessing of the measurements in order to enable the description of shear and principal strain fields within the wall. The strain fields are later compared to the crack pattern of the wall, to validate the agreement of the measurements to the wall behaviour.

2. Experimental programme

An experimental programme was devised to investigate the performance of coated DOFS to provide accurate information about a D-region's serviceability condition under cyclic loading. Therefore, a RC wall, outfitted with DOFS deployed in a multi-layer configuration was cast and cyclically loaded. The most relevant aspects of the experimental programme are described in the following.

2.1. Geometry and reinforcement layout

The specimen used in this work was a RC wall with a total width of 0.8 m and height of 0.5 m, featuring a thickness of 0.1 m. The wall was reinforced with two reinforcement grids of ∅6 mm bars at 100 mm spacing in both vertical and horizontal directions. The bottom horizontal bars of the grid were replaced by two ∅12 mm, providing extra reinforcement in the tension zone. All reinforcement was made of conventional carbon steel B500S with a nominal yield strength of 500 MPa. The wall was cast in horizontal position and plastic spacers were placed between the grid and the back side of the form to ensure a clear concrete cover of 15 mm. The geometry and reinforcement layout of the wall is presented in Fig. 1.

A premixed C32/40 class concrete was used to cast the wall element. The concrete mix had a water to cement ratio of 0.5 and 360 kg/m³ of ordinary Portland cement with a maximum aggregate size of 12 mm. Following the casting, the wall was covered with a polyethylene sheet to reduce moisture evaporation and stored in an indoor climate (20 ± 2 °C and 60 ± 10 % RH) for two weeks until it was tested.

2.2. Instrumentation

In this study, the robust reinforced fibre optic cable BRUsens V9 from Solifos, featuring an external polymeric jacket with rough surface and an inner steel reinforcement tube providing additional protection to the
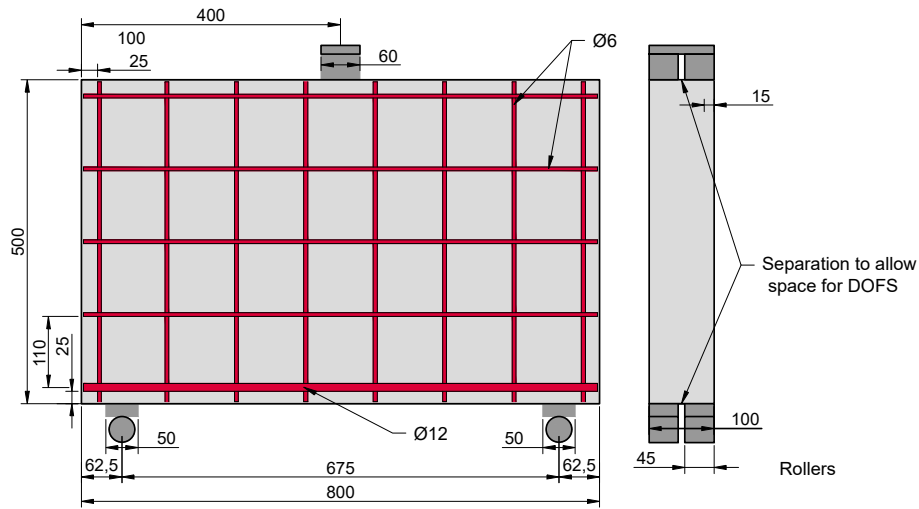
Fig. 1. Geometrical description of the concrete wall, steel reinforcement arrangement, supports and loading plate (units in mm).

fibre optic cable, was used. The multiple protective layers of the V9 cable result in an outer diameter of 3.2 mm which limit the minimum bending radius of the cable to about 60 mm when tensioned. Unlike the

125 μm-thick polyimide-coated fibres commonly used in several experimental research studies, see e.g. [49–51], the V9 cable is stiffer and can be easily handled and deployed without risk of rupture, making
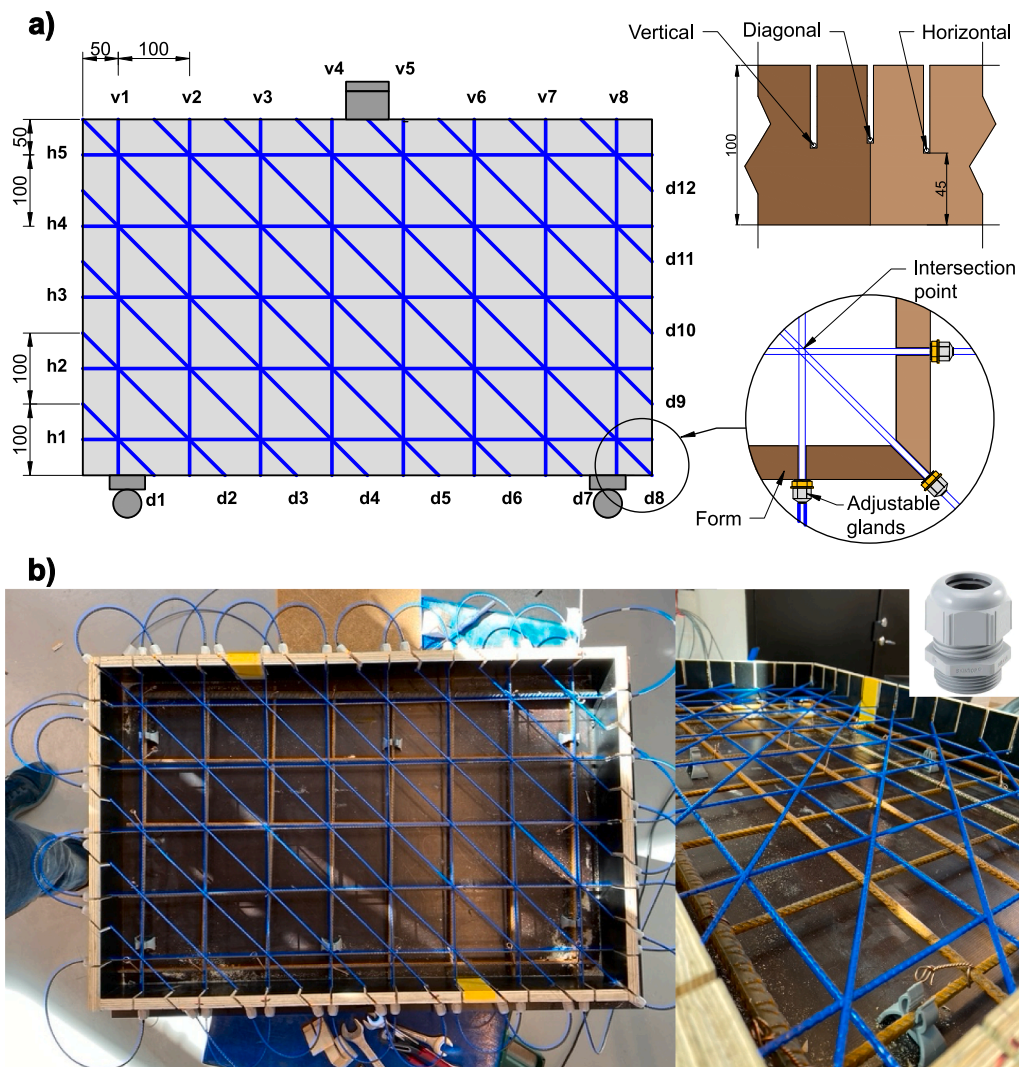

Fig. 2. (a) Optic fibre arrangement within the studied element and detail of the attachment of the Optic Fibre cable to the form (b) Final distribution of the Fibre Optic cables in multilayer configuration and detail of a cable gland. (All units in mm).

it especially suitable for both fresh and hardened concrete applications.

A single 27 m long robust DOFS was installed in a multi-layer configuration to monitor the variation of strain across the entire wall area. A total of three layers of cable, i.e., horizontal, vertical, and diagonal layer, conformed the measurement grid, see Fig. 2(a-b). All cables were arranged parallel to the back side of the specimen, starting at a height of 45 mm, what approximately corresponded to the mid-section of the concrete wall thickness. The total thickness of the sensor grid including the three directions was 9.9 mm, spanning between 45 mm and 54.9 mm in the specimen thickness, see top-right sketch in Fig. 2(a). The first and last horizontal and vertical sections, i.e., h1 and h5, and v1 and v8, were positioned parallel to the wall edges and exactly at 50 mm from the form edge. Subsequently, a regular spacing of 100 mm between cable centres was chosen to distribute the remaining sections, amounting to 5 horizontal sections, namely h1-h5, and 8 vertical sections, namely v1-v8. The third and topmost layer of the grid was formed by diagonal sections. The ends of segments d1 and d12 were placed at 100 mm from the closest corner defining an inclination of 45° with respect to the vertical and horizontal wall edges. Thereafter, the same horizontal and vertical spacing of 100 mm was used for the subsequent sections, adding up to a total of 12 diagonals, namely d1-d12. Such multi-layer configuration of the sensor grid guaranteed that all the intersections between different orientations were formed by the three directions, horizontal, vertical, and diagonal, giving a total of 40 intersection points. An important drawback of placing such grid configuration at the mid-thickness of the wall, is that the sensors had no natural support to be attached to. In order to ensure the correct position of each sensor during casting, the cable ends were clamped to the form sides by means of plastic cable glands, sometimes referred to as cord grips, see Fig. 2 for a detail. Such device enabled the application of a small prestressing force to the cable, but sufficient to keep it straight and tense during the casting process and thereby ensure its desired position in the hardened concrete, see Fig. 2(b).

The Optical Distributed Sensor Interrogator (ODiSI) 6000 series from Luna Inc. was used as data acquisition unit. This instrument offers a strain resolution of 1 $\mu\varepsilon$, a maximum strain range of $\pm$ 15000 $\mu\varepsilon$ and a sample rate that can go up to 250 Hz depending on the gauge pitch, cable and length and number of active channels. In all tests, the largest available spatial resolution between measuring points provided by the interrogator was chosen, namely 2.6 mm. This configuration provided a combined accuracy (sensor + interrogator) of $\pm$ 10 $\mu\varepsilon$, whereas the sample rate was set at 1 Hz. It is worth noting a cubic Hermite polynomial interpolation with a spatial resolution of 2 mm was performed on the measured raw data before proceeding to the analysis of the results in order to homogenize the number of gauges between different sections of the same length, without compromising the accuracy of the results.

2.3. Test setup and loading procedure

The wall was simply supported on rollers and loaded under three-point bending setup. The clear span between the centre of the supports was equal to 675 mm. The rollers placed under 50 mm wide steel plates allowed for free rotation of the supports. The load was introduced using a single actuator acting on a 60 mm wide steel distribution plate with restricted horizontal displacements. Loading was applied under displacement control using a closed-loop feedback system at a displacement rate of 0.05 mm/min. Several load cycles were performed at increasing loads reaching a final maximum load of 210 kN. The loading setup is schematically illustrated in Fig. 1 and the loading scheme is presented in Fig. 3, where three load levels of interest are indicated: 50 kN corresponding to early cracking, 125 kN corresponding to stabilized formation of bending cracks and 200 kN corresponding to the formation of the second shear crack.
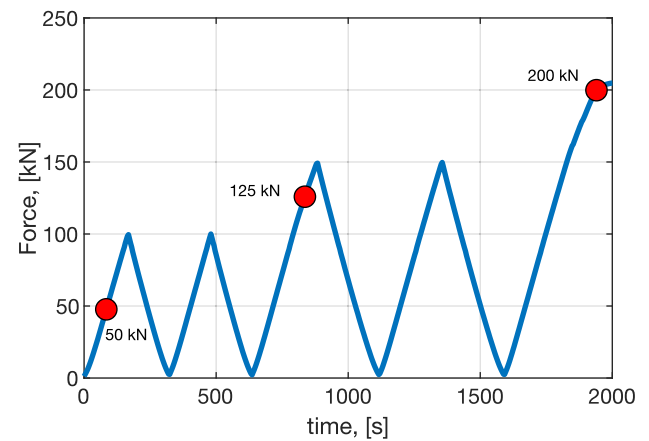

Fig. 3. Loading scheme where three selected load levels of interest (50, 125 and 200 kN) are indicated by red markers. (For interpretation of the references to colour in this figure legend, the reader is referred to the web version of this article.)

3. Results and discussion

3.1. DOFS strain profiles in reinforced concrete beams under three-point loading

As thoroughly discussed in [52], there are several factors that may have a significant impact on the robust DOFS measurements when embedded in concrete. First, the non-uniform field of strains along the wall surface will mobilize the shear response of the outer jacket in the case of perfect bonding. Second, the appearance of cracks in the concrete, both bending and shear cracks, will create steep strain gradients in the fibre cables. In that scenario, the strain transfer between the substrate material and the DOFS would be very sensitive to the properties of fibre coating/outer jacket. Deploying the sensors on the reinforcement, either by carving a notch and using adhesive or simply attaching the sensor to the surface of the bars, is a way to effectively prevent the appearance of large strain gradients and thus obtain more reliable measurements. However, the goal of this study was to develop a setup that could be used to measure strain fields in a concrete element by removing as much as possible the influence that steel reinforcement bars have on the length of sensor that is affected by intersecting cracks. Consequently, the robust DOFS was simply embedded in the concrete and fixed to the form edges. This arrangement method will provide strain measurements that should, in principle, converge quicker to the actual concrete strains away from the cracks.

3.1.1. Analysis of DOFS strains

In Fig. 4(a), the strain profiles for all the DOFS segments in the measurement grid are presented for increasing load levels. To increase the readability of the results, the strain values have been grouped into two load ranges, namely 0–100 kN and 100–200 kN, and normalised with respect to the maximum strain level of the maximum load level in each group, i.e., 100 kN and 200 kN respectively.

The results of the horizontal strains in Fig. 4(a) describe a clear initial bending behaviour of the wall, showing a concentration of compressive and tensile strains at the top and bottom of the wall, respectively. It must be noted that the presence of peaks measured at the bottom tie of the wall seems to correspond to initial bending cracks. Those peaks become more accentuated with increasing load levels as the cracking propagates further up the wall. Similar observations have been reported by several authors for DOFS applied to reinforced concrete beams [35,38,39,41], which are clearly reproduced in this experiment. Moving to the vertical strains, the results obtained are in line with the expected behaviour of the wall in such direction, i.e., the regions under both loading and above
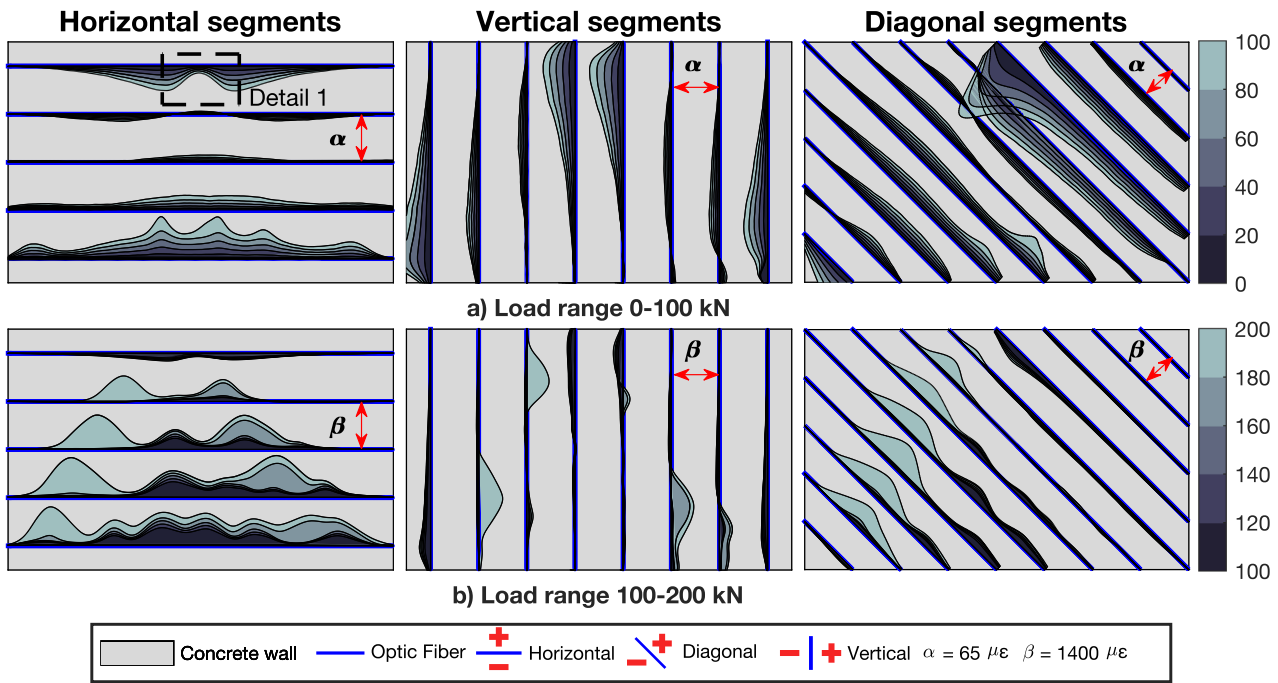
Fig. 4. Strain distributions along the fibre optic cables for load levels between a) 0–100 kN and b) 100–200 kN. For allowing a better comparison between measurements all the values were normalised with respect to the maximum strain value at 100 kN and 200 kN respectively.

reaction points described clear negative strains due to the vertical compression caused by the jack and reaction forces at the supports. Furthermore, the vertical cables located halfway between the loading and reactions points also displayed compression strains, although the concentration of strains occurred in the central part of the segment. The reason for that is that the vertical cables were clearly depicting the path of compressive strains in the concrete going from the loading plate and to the supports or, in other words, the strain peaks in the vertical cables indicated the position and width of the so-called concrete struts, see Fig. 5 for a typical example of a strut-and-tie model of the wall. Lastly, some unusual results were observed from the measurements described by the diagonal segments. The diagonal cable d9, for instance, with one of its ends right under the point load, described an important concentration of strains. The reason for this peak, which was not in agreement with the closest diagonal measurements, nor with the measurements of the closest vertical segments, was attributed to either a local clamping of

Fig. 5. Example of a strut and tie model for the tested specimen.

the cable or a local distortion due to high strains introduced by the loading plate. It must be mentioned that regardless of this observation, the values measured by the cable were not filtered in further analyses. By looking at the remaining diagonal segments, it can be noted that segments d1-d5 were in tension whereas segments d7-d12 were in compression. This is in line with the observations made for the vertical strains and the expected wall behaviour as diagonals d1-d5 were arranged perpendicular to one of the concrete struts, i.e., they were describing the corresponding splitting strains, while diagonals d7-d12 were aligned with the other concrete strut, thus showing the compressive strains of the strut. Furthermore, diagonal d6, which is somewhat between both regions described, accordingly, a compression/tension behaviour.

Regarding the analysis of the DOFS for higher loads, see Fig. 4(b), it can be seen that the measurements are consistent with the aforepresented observations. The horizontal strains still showed the bending effect on the wall with compression on the top side and tension in the bottom part of the wall. However, as the load level increased and the cracking propagated, it can be seen how the horizontal tensile strains became more dominant on the wall surface and much larger in magnitude. An observation worth mentioning is that the last two load levels revealed the presence of a major inclined crack on the right side of the wall, and the occurrence of a new, even wider inclined crack on the left side at the very last step. Those cracks correspond to the characteristic shear cracks originated in this type of element when subjected to three-point loading. The presence of shear cracks is also evident in the diagonal segments perpendicular to the concrete strut (left side), but not so clear in the vertical strains. In the former, a clear path for the shear crack can be described by the measured strain peaks, the strain of which decreased when the crack approached the loading point. Obviously, as the orientation of the cables on the right side of the wall was almost parallel to the shear crack, such crack was almost imperceptible in the recorded strains of the corresponding segments. In the vertical strains, important strain peaks were described as well when the shear cracks crossed the cables, particularly in the bottom and top part of the segments v2 and v3, respectively, for the left shear crack as well as in the bottom part of the v6 segment for the right shear crack.
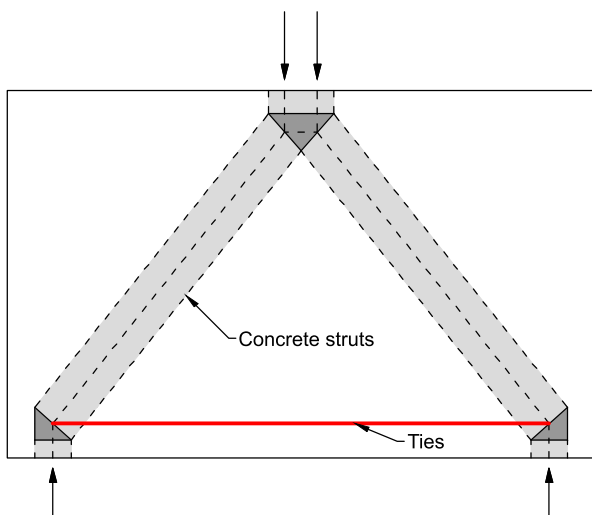
An additional observation worth noting from the horizontal strain measurements at any load level, but particularly pronounced at low load levels, is the presence of two accentuated peaks describing tensile strains right above the supports and an additional peak right below the loading plate, which reduced the compressive strains in that region. By looking closely at detail 1, highlighted in Fig. 4(a), it is possible to see that, even though the strains are negative, the measured strain magnitude became significantly smaller within a certain region around the loading plate. This behaviour is attributed to the appearance of tensile splitting strains in the transversal direction caused by the introduction of a localized point load. These splitting strains are a direct consequence to the transversal deformation due to the Poisson's effect, which is a well-known phenomenon. Based on the results shown in Fig. 6(a), this phenomenon can be well described by the DOFS measurements. Considering that the compressive strains due to the bending effect should grow bigger when approaching the loading point, the theoretical compressive strains neglecting the aforementioned Poisson's effect could be interpolated from the strains outside the influence region, see Fig. 6(a). By subtracting the actual DOFS measurements to the interpolated values, it is therefore possible to isolate the theoretical contribution due to Poisson's transverse deformation in the specific region, see Fig. 6(b). Subsequently, from these strains the applied force under the loading plate could be estimated according to Eq. (1) and thereafter compared to the actual applied force:

$$F_{app} = \frac{1}{v} \bullet \int_{l_0}^{l_1} (\varepsilon_{h_m} - \varepsilon_{h_{int}})dx \bullet E_c \bullet t_{wall} \tag{1}$$

where ε_{h_m} is the measured horizontal strain by the DOFS, $\varepsilon_{h_{int}}$ is the strain interpolated from the measured data outside the affected region, $l_1 = 312mm$ and $l_2 = 480mm$ are the limits of the affected zone, $E_c = 26000MPa$, is the concrete modulus of elasticity and t_{wall} is the wall thickness, 100 mm. Finally, v represents the concrete's Poisson's ratio which for hardened concrete usually ranges between 0.15 and 0.25 [53] and in this work was chosen to be 0.18 as the age of the concrete was only 14 days at the time of testing.

Fig. 7 shows a direct comparison between the measured applied force and the force calculated by Eq. (1). As observed, the agreement between both values for the different load levels from 20 to 100 kN is excellent being the difference between them in all cases lower than 10 %. That supports the hypothesis that the fibre optic cable installed under the loading point was able to capture accurately the splitting strains due to the introduction of the load and therefore such information can be used
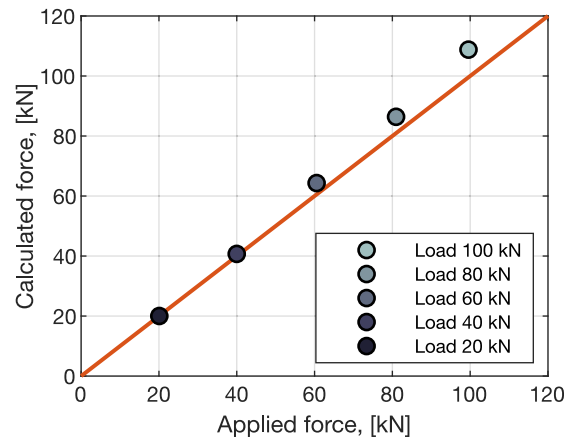

Fig. 7. Indirectly calculated force in the element by the proposed method compared to the actual applied load.

to reach better understanding of the structural behaviour of D-regions and propose better design methods.

3.1.2. Crack detection by DOFS

As discussed by several authors, the distributed nature of the strain measurements based on Rayleigh scattering provides a straightforward way to identify the position of cracks, which appear as well-defined peaks in the strain profiles [39]. In addition, thanks to their smoother signal output, coated DOFS embedded in concrete do not require complex post-processing algorithms to remove strain reading anomalies, commonly present when using sensors without a robust outer jacket [38]. It is worth mentioning, however, that most of the available studies have focused on beam elements with sensors installed on the steel reinforcement. As discussed in Section 3.1.1, the strain profiles presented in Fig. 4 also describe a similar output as previously reported in the literature [38,40,50], highlighting the presence of cracks. Consequently, such strains can be used to unambiguously identify the onset of cracking as well as to follow the propagation of cracks. However, it must be noted that unlike other works where the sensors were somehow supported on the steel bars, in the present work sensors were deployed in the mid-plane section of the wall, without any physical support. Consequently, the calculation of crack widths as proposed by several authors, [34,38,41], is in principle not applicable since the strain measured by the sensors at the cracks does not correspond to the steel strain. Thus, the validation of existing methodologies or the development of new ones is needed to perform such calculations using the proposed setup. In order to highlight the potential of the presented fibre deployment method, in Fig. 8 the final crack pattern of the wall for a load of 200 kN is compared to the strain measurements for the same load level. As observed, the results display a very good agreement, which in turn upholds the ability of DOFS to detect cracking in elements other than beams, and particularly for D-regions.

3.2. Postprocessing of DOFS strain for visualization of 2D strain fields

3.2.1. Interpolation of DOFS strains

In order to facilitate and enhance the visualization of strain results for elements other than beams, where strains may distribute in large surfaces and in a more complex manner, the measurements obtained by the different cable segments can be used to create heat maps of strains in every direction. To move from discrete data at the different cable positions to continuous data across the wall surface, data interpolation is required. For the interpolation, it was assumed that the variation of the strain between two consecutive segments in the same direction was linear. Subsequently, a regular grid interpolation algorithm was applied to the data aiming to obtain uniformly distributed values of strain every
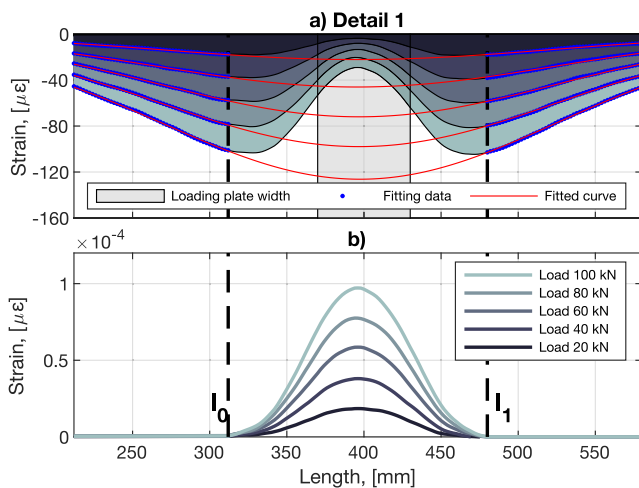

Fig. 6. (a) Strain profile measured by DOFS under the loading plate. (b) Tensile transversal strains capture by DOFS due to the load introduction in the wall element calculated as the difference between interpolated and measured strains.
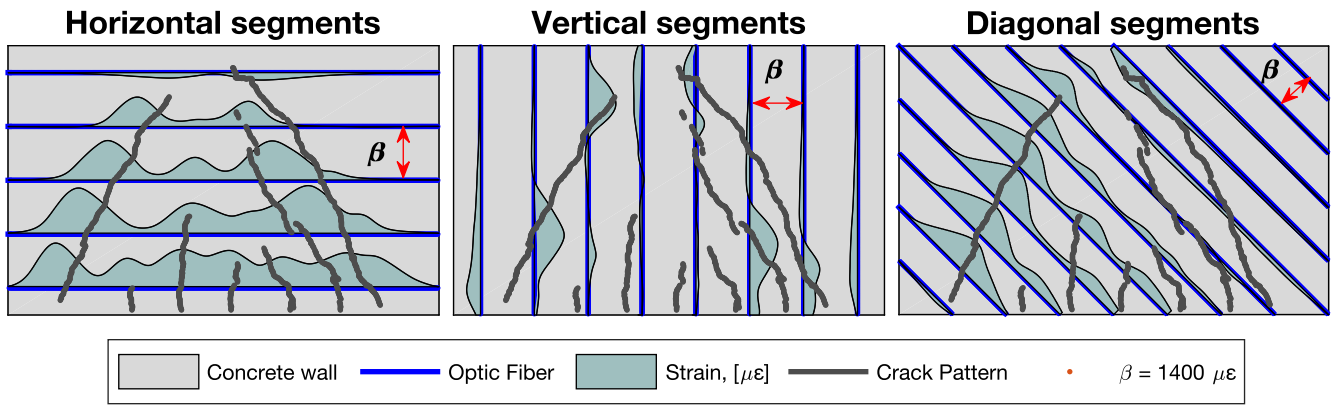
Fig. 8. Measured strain at 200 kN and corresponding crack pattern.

20 mm in all directions, i.e., horizontal (global X), vertical (global Y) and diagonal (XY direction). Fig. 9 shows the interpolated data for the three load levels of interest indicated in Fig. 3, namely 50, 125 and 200 kN, which corresponded to a low load stage at early cracking, a load stage with full development of bending cracks and lastly a load step where all shear cracks were fully formed. These load levels were chosen to showcase the ability of DOFS to detect and follow cracks of different origin, namely, bending cracks, which are transversal to the horizontal fibre and thus easy to detect, but also shear cracks which run diagonally

and could be, in principle, harder to capture with DOFS, as their nature only allows for the strain measurement along the sensor path. However, it can be clearly seen that the interpolated values provide a comprehensive and richer visualization of the strains enabling the tracking of crack development.

Other existing technologies such as Digital Image Correlation (DIC), also allow obtaining similar results, where strain fields and crack development can be followed during testing. It is also important to highlight that like for DIC results, the interpolated strain maps presented
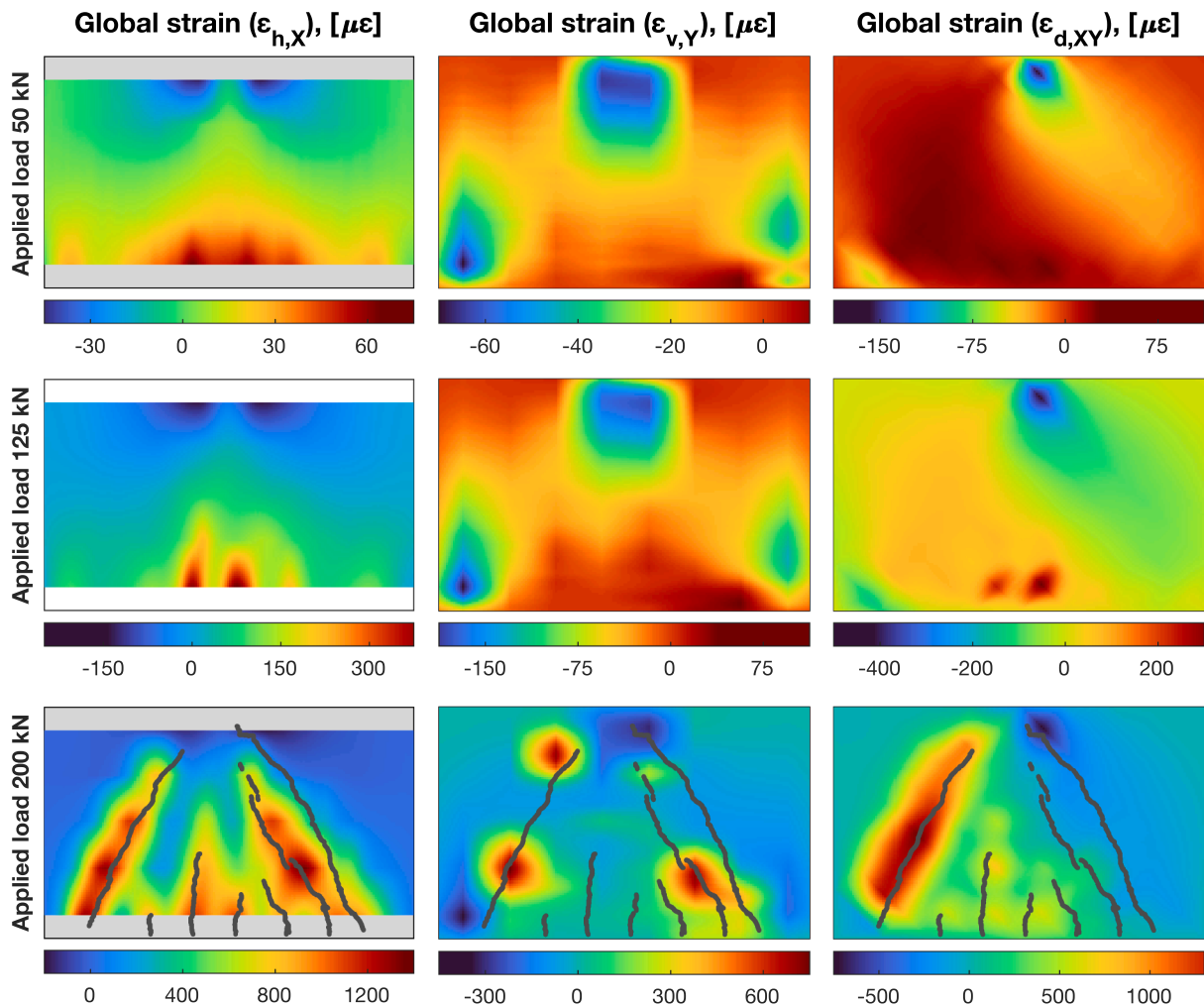

Fig. 9. Interpolated strain fields in the three directions of the arranged grid, horizontal, vertical, and diagonal at the indicated load levels in Fig. 3. Note that the colour scale is different for every subfigure.

in Fig. 9 and subsequent figures, do not represent the actual mechanical strain of the material, which for concrete should be equal to zero at the cracks. Instead, the presented values are an idealization of the concrete strains assuming the material as a continuum, where the discontinuity of the displacement field at the cracks is smeared over a certain distance which is converted into a fictious strain. An advantage of DIC is that the influence length over which the crack opening is distributed is generally smaller, resulting in a better localization of cracks and more accurate crack patterns. However, DIC results are limited to the surface of the element and the resolution of commonly available cameras is usually not sufficient to provide an accurate description of concrete strains in large elements. Conversely, DOFS are not sensitive to the element size since the resolution of the sensor is independent of its length, allowing for the measurement of strain fields to be scaled up to elements of any size.

3.2.2. Calculation of principal strains

Even though the results presented and discussed in section 3.2.1 demonstrate that the described methodology enables a comprehensive analysis of the strain fields within the wall, a common and more intuitive approach to investigate the structural behaviour of D-regions is the study of principal strains. The traditional approach to experimentally measure principal strains in a concrete element has been the use of rosette strain gauges, either conventional or based on FBG-built rosettes, see [54–58]. This type of gauges enables the measurement of global strains in three directions, namely X, Y and XY (usually placed at 45° from the X direction) or what is the same ε_X, ε_Y and ε_{XY}. Using Eq. (2), which is only applicable for an angle of 45° between XY and X, it is possible to obtain the shear strains, and consequently the magnitude and angle with respect to the global direction X of the principal strains:

$$\varepsilon_{max} = \frac{1}{2}\left[\varepsilon_X + \varepsilon_Y + \gamma_{max}\right]$$

$$\varepsilon_{min} = \frac{1}{2}\left[\varepsilon_X + \varepsilon_Y - \gamma_{max}\right]$$

$$\theta = \frac{1}{2}\tan^{-1}\left(\frac{\varepsilon_X + \varepsilon_Y - 2 \bullet \varepsilon_{XY}}{\varepsilon_X - \varepsilon_Y}\right)$$

$$\gamma_{max} = \sqrt{2\bullet\left((\varepsilon_X - \varepsilon_{XY})^2 + (\varepsilon_{XY} - \varepsilon_Y)^2\right)} \quad (2)$$

Using Eq. (2), the principal strains ε_{max} and ε_{min} can be directly calculated at the 40 intersection points between the horizontal, vertical and diagonal cables, where actual values of the strains in three directions were measured, namely $\varepsilon_h = \varepsilon_X$, $\varepsilon_v = \varepsilon_Y$ and $\varepsilon_d = \varepsilon_{XY}$ according to the wall's global coordinate system. However, if only the 40 intersection points were used, the resolution of the grid would be very low (although still much higher than with traditional approaches based on rosette strain gauges). Additionally, using only the intersection points would not make use of the full potential of the distributed measuring nature of the DOFS. Therefore, in this work it was suggested to use the same interpolated grid used to create the heat maps shown in Fig. 9 in order to increase the number of points with information of the principal strains and the corresponding angles. Accordingly, in Fig. 10 the principal strains ε_{max} and ε_{min} together with the shear strains, γ_{max}, are shown for the same load levels as in Fig. 9.

Several important observations are to be noted from Fig. 10. First, the crack distribution is generally better described by the maximum principal strain, ε_{max}, than by any of the global components. However, there are obvious similarities between the ε_{max} and ε_h, because the largest tensile strains in the wall were predominantly horizontal.
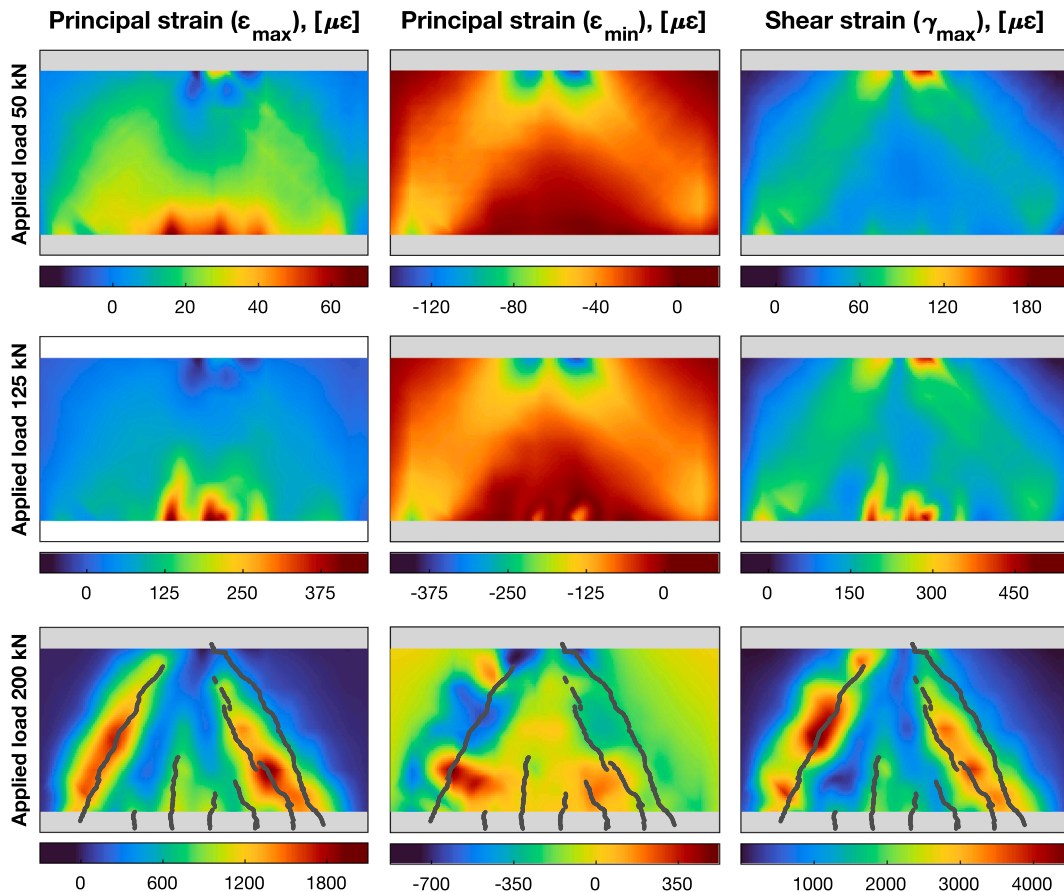

Fig. 10. Calculated principal and shear strain fields from the interpolated strains presented in Fig. 9 at the same load levels.

Moreover, the minimum principal strains, ε_{min}, allowed for the visualization of the load paths from the loading point to the reaction plates in an evident way, showing very markedly the two concrete struts formed. Additionally, looking closely to the principal strain, ε_{min}, for a load level of 200 kN, the heat map reveals a secondary strut and tie mechanism right after the formation of the left shear crack. Such secondary strut-and-tie mechanisms are a known phenomenon, but to the authors' knowledge it has never been experimentally measured and presented as done in the present work. Lastly, the shear strains shown in Fig. 10, display distinctly the regions in the wall subjected to higher shear strains, indicating at a very early stage the position of the shear cracks that occurred at higher load levels.

Finally, if the principal strains ε_{max} and ε_{min} are plotted together with the angle formed to the global axis X, it is possible to show in a more intuitive way the strain fields at different load levels. Fig. 11 illustrates in a clear manner how the variation of the load paths occurred in the wall for increasing load levels. Similarly, for the last load step, Fig. 11
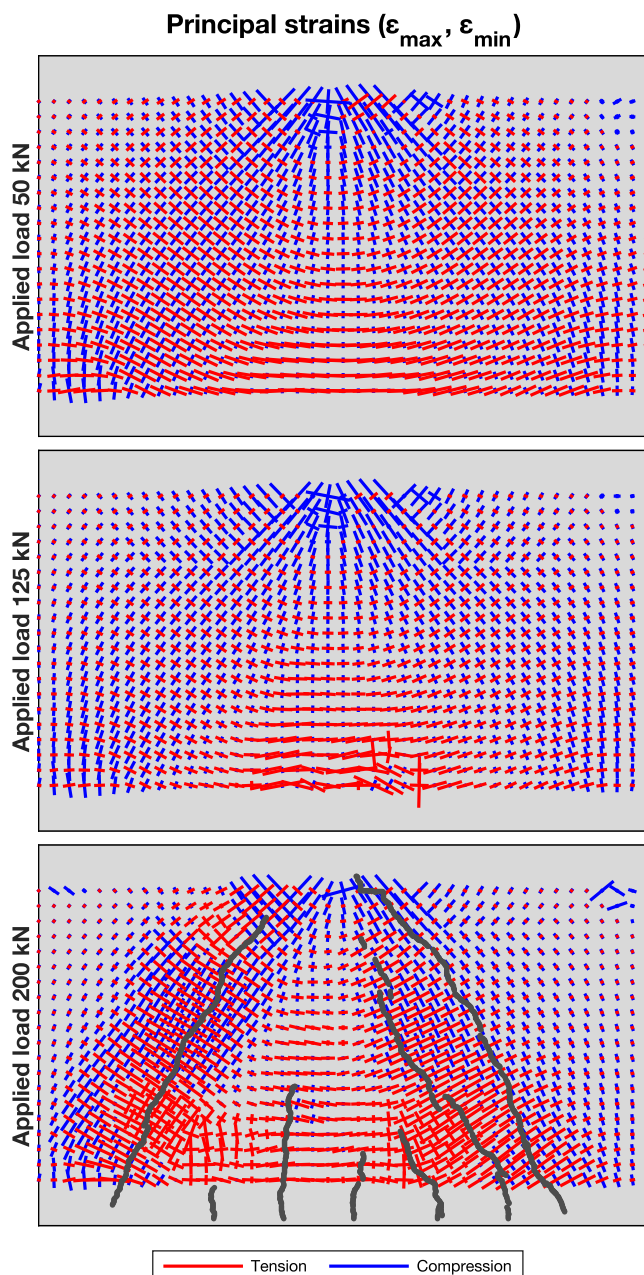
depicts the formation of the aforementioned secondary strut-and-tie mechanism in a precise way.

4. Conclusions

This article investigated the analysis of D-regions by DOFS based on Rayleigh backscattering. A wall element was cast with a robust fibre optic sensing cable deployed in a multi-layer configuration at the mid-section of the wall. The wall was subjected to cyclic loading under three-point loading while the strains were continuously measured. The main conclusions drawn from this study are the following:

- The proposed methodology for the deployment of optical fibre sensors in D-regions proved successful for the study of two-dimensional strain fields yielding superior results in terms of data richness compared to conventional techniques.
- The direct measurements for the three global directions, ε_h, ε_v and ε_d, showed relevant information of crack development and local effects. The accuracy and resolution of the DOFS is such that it enabled the measurement of transversal deformation due to the load introduction. This information could be even used to back calculate the applied load.
- In line with previously reported research focused on reinforced concrete beams, the strain measurements could be also used to determine the crack onset and to track the crack development in a wall element. However, using the proposed methodology in which the sensors are placed at the mid-thickness of the wall instead of being installed on the steel reinforcement, requires the development of new methods to calculate crack widths.
- The interpolation of DOFS measurements assuming a linear variation of strains between consecutive segments proved to be a suitable and effective way to obtain a comprehensive view of the data while offering flexibility in the output resolution. For the studied element and the load configuration used, a spacing of 100 mm between segments in the different directions was deemed adequate to describe the element behaviour accurately. However, a detailed study of the limits of the sensor spacing is of interest to minimise the amount of cable necessary.
- The proposed method for the fibre optic deployment in a multilayer configuration following the global directions X, Y and XY, enabled the direct calculation of the principal strain from the measurements at 40 intersection points. However, the amount of data could be drastically increased by combining the benefits of distributed strain sensing and the proposed interpolation approach, which yielded detailed heat maps of the principal strains. The computation of principal and shear strains in this way allowed for the experimental study of D-regions in an unprecedented way.
- The visualization of shear strains enabled the early detection and localization of the regions where later shear cracks would form at much higher load levels. Likewise, the visualization of principal strains enabled the clear identification of concrete struts at any load level as well as the identification of a secondary strut-and-tie mechanism formed after the second shear crack occurred. To the authors' knowledge this has not been previously experimentally captured and shows the great potential of the presented method for study of the structural behaviour of reinforced concrete walls and D-regions in general.

Funding

Principal strains (ε_{max}, ε_{min})

Fig. 11. Combined plot for the principal strain fields at the refence load levels.

Declaration of Competing Interest

The authors declare that they have no known competing financial interests or personal relationships that could have appeared to influence the work reported in this paper.

Data availability

The data is publish in a national repository at Sweden with a corresponding DOI indicated in the document. The data generated in this work can be accessed and downloaded under Open Data Commons Public Domain Dedication and License (PDDDL 1.0) agreement, from the "Svensk nationell datatjänst" (SND) public servers [59].

Appendix A. Supplementary data

Supplementary data to this article can be found online at https://doi.org/10.1016/j.engstruct.2022.115562.

References

[1] Marti P. Basic Tools of Reinforced Concrete Beam Design. J Proc 1985;82(1):46–56. https://doi.org/10.14359/10314.
[2] Schlaich J, Schiifer K. Design and detailing of structural concrete using strut-and-tie models. Struct Eng 1991;69(6).
[3] Schlaich J, Schaefer K, Jennewein M. TOWARD A CONSISTENT DESIGN OF STRUCTURAL CONCRETE. PCI J 1987;32(3):74–150. https://doi.org/10.15554/PCIJ.05011987.74.150.
[4] Drucker DC. On structural concrete and the theorems of limit analysis. Publications 1961;21:49–59.
[5] Nielsen MP, Braestrup MW, Jensen BC, Bach F. Concrete plasticity, beam shear - Shear in joints - Punching shear. Concrete Plasticity 1978.
[6] Muttoni, A., "The Applicability of the Theory of Plasticity in the Design of Reinforced Concrete," ("Die Andwendbarkeit der Plastizitätstheorie in der Bemessung von Stahlbeton"), Institut für Baustatik und Konstruction, Bericht, No. 176, ETH Zürich, 1989, 159 pp. (in German).
[7] Despot, Z., "Finite Element Method and Plasticity Theory for the Dimensioning of Reinforced Concrete Disks," ("Methode der finite Elemente und Plastizitätstheorie zur Bemessung von Stahlbetonscheiben"), PhD thesis, ETH Zürich, 1995, 121 pp. (in German).
[8] Ruiz MF, Muttoni A. On Development of Suitable Stress Fields for Structural Concrete. Structral J 2007;104(4):495–502. https://doi.org/10.14359/18780.
[9] Muttoni A, Ruiz MF, Niketic F. Design versus Assessment of Concrete Structures Using Stress Fields and Strut-and-Tie Models. Structral J 2015;112(5):605–16. https://doi.org/10.14359/51687710.
[10] M. Číhal, J. Kabeláč, M. Konečný, and L. Juříček, "Serviceability Limit State Evaluation in Discontinuity Regions," 2019, doi: 10.4028/www.scientific.net/SSP.292.203.
[11] Chen H, Yi WJ, Hwang HJ. Cracking strut-and-tie model for shear strength evaluation of reinforced concrete deep beams. Eng Struct 2018;163:396–408. https://doi.org/10.1016/j.engstruct.2018.02.077.
[12] Ali SRM, Saeed JA. Shear capacity and behavior of high-strength concrete beams with openings. Eng Struct 2022;264:114431. https://doi.org/10.1016/J.ENGSTRUCT.2022.114431.
[13] Zhang N, Tan KH. Size effect in RC deep beams: Experimental investigation and STM verification. Eng Struct 2007;29(12):3241–54. https://doi.org/10.1016/J.ENGSTRUCT.2007.10.005.
[14] Walraven J, Lehwalter N. Size effects in short beams loaded in shear. ACI Mater J 1994;91(5):585–93. https://doi.org/10.14359/4177.
[15] Lu WY, Lin IJ, Hwang SJ. Shear strength of reinforced concrete corbels. Mag Concr Res 2009;61(10):807–13. https://doi.org/10.1680/MACR.2008.61.10.807.
[16] "The Behaviour of Reinforced Concrete Continuous Deep Beams | TU Delft Repositories." https://repository.tudelft.nl/islandora/object/uuid:812fac53-dd91-4d3a-bd19-5743a3783798 (accessed Jul. 21, 2022).
[17] Abadel A, et al. Experimental study of shear behavior of CFRP strengthened ultra-high-performance fiber-reinforced concrete deep beams. Case Stud Constr Mater 2022;16. https://doi.org/10.1016/j.cscm.2022.e01103.
[18] Marzec I, Tejchman J. Experimental and numerical investigations on RC beams with stirrups scaled along height or length. Eng Struct 2022;252. https://doi.org/10.1016/j.engstruct.2021.113621.
[19] Arabzadeh A, Hizaji R, Yang TY. Experimentally studying and development of curved STM to predict the load capacity and failure mode of fixed-ended RC deep beams. Structures 2020;23:289–303. https://doi.org/10.1016/j.istruc.2019.09.011.
[20] J. L. Jewett and J. v. Carstensen, "Experimental investigation of strut-and-tie layouts in deep RC beams designed with hybrid bi-linear topology optimization," *Eng Struct*, vol. 197, Oct. 2019, doi: 10.1016/j.engstruct.2019.109322.
[21] Casas JR, Cruz PJS. Fiber Optic Sensors for Bridge Monitoring. J Bridg Eng 2003;8(6):362–73. https://doi.org/10.1061/(asce)1084-0702(2003)8:6(362).

[22] Majumder M, Gangopadhyay TK, Chakraborty AK, Dasgupta K, Bhattacharya DK. Fibre Bragg gratings in structural health monitoring-Present status and applications. Sens Actuators A Phys 2008;147(1):150–64. https://doi.org/10.1016/j.sna.2008.04.008.
[23] Barrias A, Casas JR, Villalba S. A review of distributed optical fiber sensors for civil engineering applications. Sensors (Switzerland) 2016;16(5):pp. https://doi.org/10.3390/s16050748.
[24] Güemes A, Fernández-López A, Soller B. Optical Fiber Distributed Sensing - Physical Principles and Applications. Structural Health Monitoring: An International Journal 2010;9(3):233–45. https://doi.org/10.1177/1475921710365263.
[25] F. Gyger, E. Rochat, S. Chin, M. Niklès, and L. Thévenaz, "Extending the sensing range of Brillouin optical time-domain analysis up to 325 km combining four optical repeaters," in *23rd International Conference on Optical Fibre Sensors*, Jun. 2014, p. 91576Q. doi: 10.1117/12.2059590.
[26] Rodriguez G, Casas JR, Villalba S. SHM by DOFS in civil engineering: a review. Structural Monitoring and Maintenance 2015;2(4):357–82. https://doi.org/10.12989/smm.2015.2.4.357.
[27] M. Francesco Bado, J. R. Casas, A. Editors, K. Benzarti, and P. Antunes, "A Review of Recent Distributed Optical Fiber Sensors Applications for Civil Engineering Structural Health Monitoring," *Sensors 2021, Vol. 21, Page 1818*, vol. 21, no. 5, p. 1818, Mar. 2021, doi: 10.3390/S21051818.
[28] A. L. Kalamkarov *et al.*, "Strain measurement in a concrete beam by use of the Brillouin-scattering-based distributed fiber sensor with single-mode fibers embedded in glass fiber reinforced polymer rods and bonded to steel reinforcing bars," *Applied Optics, Vol. 41, Issue 24, pp. 5105-5114*, vol. 41, no. 24, pp. 5105–5114, Aug. 2002, doi: 10.1364/AO.41.005105.
[29] D. Meng, F. Ansari, and X. Feng, "Detection and monitoring of surface micro-cracks by PPP-BOTDA," *Applied Optics, Vol. 54, Issue 16, pp. 4972-4978*, vol. 54, no. 16, pp. 4972–4978, Jun. 2015, doi: 10.1364/AO.54.004972.
[30] Imai M, Nakano M, Kono T, Ichinomiya T, Miura S, Mure M. Crack Detection Application for Fiber Reinforced Concrete Using BOCDA-Based Optical Fiber Strain Sensor. J Struct Eng 2010;136(8):1001–8. https://doi.org/10.1061/(ASCE)ST.1943-541X.0000195.
[31] Y. Bao and G. Chen, "Strain distribution and crack detection in thin unbonded concrete pavement overlays with fully distributed fiber optic sensors," *https://doi.org/10.1117/1.OE.55.1.011008*, vol. 55, no. 1, p. 011008, Oct. 2015, doi: 10.1117/1.OE.55.1.011008.
[32] Barrias A, Casas JR, Villalba S. Application study of embedded Rayleigh based Distributed Optical Fiber Sensors in concrete beams. Procedia Eng 2017;199:2014–9. https://doi.org/10.1016/J.PROENG.2017.09.466.
[33] Davis MB, Hoult NA, Bajaj S, Bentz EC. Distributed Sensing for Shrinkage and Tension-Stiffening Measurement. Structral J 2017;114(3):753–64. https://doi.org/10.14359/51689463.
[34] R. Regier and N. A. Hoult, "Concrete deterioration detection using distributed sensors," *https://doi.org/10.1680/stbu.13.00070*, vol. 168, no. 2, pp. 118–126, Sep. 2015, doi: 10.1680/STBU.13.00070.
[35] Henault JM, et al. Quantitative strain measurement and crack detection in RC structures using a truly distributed fiber optic sensing system. Constr Build Mater 2012;37:916–23. https://doi.org/10.1016/J.CONBUILDMAT.2012.05.029.
[36] Poldon JJ, Hoult NA, Bentz EC. Distributed Sensing in Large Reinforced Concrete Shear Test. Structral J 2019;116(5):235–46. https://doi.org/10.14359/51716765.
[37] Brault A, Hoult N. Monitoring Reinforced Concrete Serviceability Performance Using Fiber-Optic Sensors. Structral J 2019;116(1):57–70. https://doi.org/10.14359/51710870.
[38] Berrocal CG, Fernandez I, Bado MF, Casas JR, Rempling R. Assessment and visualization of performance indicators of reinforced concrete beams by distributed optical fibre sensing. Struct Health Monit 2021;20(6):3309–26. https://doi.org/10.1177/1475921720984431.
[39] Berrocal CG, Fernandez I, Rempling R. Crack monitoring in reinforced concrete beams by distributed optical fiber sensors. Struct Infrastruct Eng 2021;17(1):124–39. https://doi.org/10.1080/15732479.2020.1731558.
[40] Fernandez I, Berrocal CG, Rempling R. Long-term performance of distributed optical fiber sensors embedded in reinforced concrete beams under sustained deflection and cyclic loading. Sensors 2021;21(19). https://doi.org/10.3390/S21196338.
[41] Fernandez I, Gill Berrocal C, Almfeldt S, Rempling R. Monitoring of new and existing stainless-steel reinforced concrete structures by clad distributed optical fibre sensing. Struct Health Monit 2022. https://doi.org/10.1177/14759217221081149.
[42] G. Rodriguez, J. R. Casas, and S. Villalba, "Shear crack pattern identification in concrete elements via distributed optical fibre grid," *https://doi.org/10.1080/15732479.2019.1640256*, vol. 15, no. 12, pp. 1630–1648, Dec. 2019, doi: 10.1080/15732479.2019.1640256.
[43] Rodriguez G, Casas JR, Villalba S. Shear crack width assessment in concrete structures by 2D distributed optical fiber. Eng Struct 2019;195:508–23. https://doi.org/10.1016/J.ENGSTRUCT.2019.05.079.
[44] Mata-Falcón J, Haefliger S, Lee M, Galkovski T, Gehri N. Combined application of distributed fibre optical and digital image correlation measurements to structural concrete experiments. Eng Struct 2020;225:111309. https://doi.org/10.1016/J.ENGSTRUCT.2020.111309.
[45] Poldon JJ, Hoult NA, Bentz EC. Understanding Reinforcement Behavior Using Distributed Measurements of Shear Tests. Structral J 2021;118(3):255–66. https://doi.org/10.14359/51730537.

[46] Poldon JJ, Bentz EC, Hoult NA. Assessing beam shear behavior with distributed longitudinal strains. Struct Concr 2022;23(3):1555–71. https://doi.org/10.1002/suco.202100730.

[47] de B. N. and K. C., "Monitoring of Piles and Diaphragm Walls with Distributed Fibre Optic Sensors," in *Piling 2020*, pp. 497–502. doi: 10.1680/pttc.65048.497.

[48] N. de Battista, M. A. Bravo-Haro, and C. Kechavarzi, "Fibre Optic Monitoring Systems in the Cambridge University Civil Engineering Building," pp. 78–87, 2023, doi: 10.1007/978-3-031-07258-1_9.

[49] Bado MF, Casas JR, Dey A, Berrocal CG. Distributed optical fiber sensing bonding techniques performance for embedment inside reinforced concrete structures. Sensors (Switzerland) 2020;20(20):1–23. https://doi.org/10.3390/s20205788.

[50] Bado MF, et al. Characterization of concrete shrinkage induced strains in internally-restrained RC structures by Distributed Optical Fiber Sensing. Cem Concr Compos 2021.

[51] Rodriguez G, Casas JR, Villalba S. Shear crack width assessment in concrete structures by 2D distributed optical fiber. Eng Struct 2019;195(May):508–23. https://doi.org/10.1016/j.engstruct.2019.05.079.

[52] Berrocal CG, Fernandez I, Bado MF, Casas JR, Rempling R. Assessment and visualization of performance indicators of reinforced concrete beams by distributed optical fibre sensing. Struct Health Monit 2021. https://doi.org/10.1177/1475921720984431.

[53] by M. Anson and K. Newman, "The effect of mix proportions and method of testing on Poisson's ratio for mortars and concretes.".

[54] Romera JM, Marcos I, Skaf M, Ortega-López V. An alternative experimental methodology to determine the diagonal cracking resistance of steel-reinforced concrete beams. Eng Struct 2021;244:112741. https://doi.org/10.1016/J.ENGSTRUCT.2021.112741.

[55] H. H. Hussein, S. M. Sargand, Y. Zhu, I. Khoury, and F. T. al Rikabi, "Experimental and numerical investigation on optimized ultra-high performance concrete shear key with shear reinforcement bars," *Structures*, vol. 40, pp. 403–419, Jun. 2022, doi: 10.1016/J.ISTRUC.2022.04.037.

[56] de Sutter S, Verbruggen S, Tysmans T. Shear behaviour of hybrid composite-concrete beams: Experimental failure and strain analysis. Compos Struct 2016;152:607–16. https://doi.org/10.1016/J.COMPSTRUCT.2016.05.075.

[57] Sun A, Wu Z, Huang H. Development and evaluation of PPP-BOTDA based optical fiber three dimension strain rosette sensor. Optik - International Journal for Light and Electron Optics 2013;124(8):744–6. https://doi.org/10.1016/J.IJLEO.2012.01.028.

[58] M. Vilela, P. Ferdinand, S. Rougeault, and S. Magne, "State-of-strain evaluation with fiber Bragg grating rosettes: application to discrimination between strain and temperature effects in fiber sensors," *Applied Optics, Vol. 36, Issue 36, pp. 9437-9447*, vol. 36, no. 36, pp. 9437–9447, Dec. 1997, doi: 10.1364/AO.36.009437.

[59] Fernandez I, Berrocal CG, Rempling R. Two-dimensional strain field data from Distributed Optical Fibre Sensors in a wall element. Swedish National Data Service 2022. https://doi.org/10.5878/r6t3-5w03.